Engineering Geology 350 (2025) 107988

Contents lists available at ScienceDirect

Engineering Geology

journal homepage: www.elsevier.com/locate/enggeo

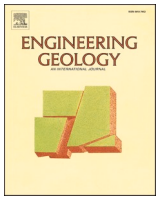

# Flash flood impacts and vulnerability mapping at catchment scale: Insights from southern Apennines

Giovanni Forte [a,*], Melania De Falco [a], Antonio Santo [a], Dipendra Gautam [b], Nicoletta Santangelo [c]

[a] DICEA, Dipartimento d'Ingegneria Civile, Edile e Ambientale; Università degli Studi di Napoli Federico II. Via Claudio 21, 80125 Napoli, Italy
[b] Earthquake Engineering Research Center, Faculty of Civil and Environmental Engineering, University of Iceland, Selfoss, Iceland
[c] DISTAR, Dipartimento di Scienze della Terra, dell'Ambiente e delle Risorse; Università degli Studi di Napoli Federico II. Via Vicinale Cupa Cintia, 21, 80126 Napoli, Italy

ARTICLE INFO

*Keywords:*
Flood vulnerability
Nonstructural element
Fragility function
Flash floods
Debris impact
Southern Apennines

ABSTRACT

Flash floods are frequent natural hazard events in many parts of the world. Generally, they occur in small catchments drained by torrential streams that feed alluvial fans or fan deltas. In the Mediterranean region, these phenomena are particularly common during the spring and autumn seasons, often causing significant damage to buildings, infrastructures, agriculture, and sometimes resulting in fatalities and injuries. To better understand and manage the potential consequences of these events on physical systems, probabilistic damage quantification is essential. Fragility functions, which describe the probability of reaching or exceeding a specific damage state based on an intensity measure, are valuable tools for assessing damage conditioned on the intensity of a natural hazard. While such curves are widely reported and extensively applied, there is a notable lack of interdisciplinary methodologies for their development and integration into broader risk management frameworks. This gap often leaves initiatives such as flood insurance premium planning, probabilistic loss estimation, and flood risk management reliant on uninformed or generic tools.

This study proposes an interdisciplinary approach to developing flood fragility functions using post-event flash flood damage data. The event that occurred on 14–15 October 2015 in Solopaca – Paupisi area (Benevento, Italy) is adopted as the case study. The reactivation of alluvial fan lobes is analyzed together with the recorded rainfalls. It is based on the processing of post-event field data acquired with classical and remote sensing technologies such as UAV imagery. Impact mapping is then conducted to depict the spatial extent of the flash flood. The event is then characterized in terms of inundation depth and thickness of mobilized material and grain size distribution. The area of the event and the thickness of the deposits are considered to estimate the transported solid volumes. Finally, the damage incurred to buildings and respective inundation depth is assembled to construct flash flood fragility functions. The outcomes of this study can be used in numerical flow model calibration and validation as well as flash flood risk assessment and management initiatives. The fragility functions developed in this study can serve as a tool for loss assessment, resilient construction prioritization, and insurance premium planning. The interdisciplinary approach developed and implemented in this study will be insightful to many other regions across the world in terms of flash flood mitigation planning.

## 1. Introduction

Flash floods are sudden and intense floods characterized by high peak discharges, caused by severe localized thunderstorms (IAHS-UNESCO-WMO, 1974). The term "flash" emphasizes the rapid rise in stream discharge, which peaks within a few hours after the causative storm, leaving minimal time for warning (Georgakakos, 1992; Creutin and Borga, 2003; Collier, 2007). These events are frequent natural hazards in many parts of Europe (Gaume et al., 2009) that generally occur in small catchments, drained by torrential streams, often feeding alluvial fans or fan deltas.

In the Mediterranean region, flash floods are most common during the spring and autumn seasons (Santangelo et al., 2021). The affected basins are typically characterized by high relief energy, sometimes

* Corresponding author.
*E-mail address:* giovanni.forte@unina.it (G. Forte).

https://doi.org/10.1016/j.enggeo.2025.107988
Received 3 October 2024; Received in revised form 23 January 2025; Accepted 26 February 2025
Available online 28 February 2025

located in coastal areas, as observed in Italy, France, Spain, and Greece (Camarasa and Tilford, 2002; Gaume et al., 2009; Alessio et al., 2013; Ruiz-Villanueva et al., 2013; Vennari et al., 2016). These floods can cause significant damage to built environments, including structures, infrastructure, and agriculture, while also posing substantial risk to human lives (Barredo, 2007; Lumbroso and Gaume, 2012; Gautam and Dong, 2018; Dolojan et al., 2023). The magnitude of a flash flood depends on multiple factors such as rainfall intensity, size and slope of the basins, concentration times, and the presence of erodible materials in the channel. Peak discharge is often used to quantify the flood magnitude; however, direct measurements are often impractical in small mountainous catchments (Benito and Thorndycraft, 2004). Instead, post-flood surveys are the most effective approach to characterize flash flood events as they permit to collect detailed field data on flow depth, transported material, and damage (Gaume and Borga, 2008). Field data are also critical for constructing fragility functions, which link hazard intensity to the degree of damage sustained by exposed elements (Luo et al., 2020; Yan et al., 2020; Chen et al., 2021). Such functions are essential for assessing vulnerability, which is often expressed on a scale from no loss (0) to total loss (1) (Uzielli et al., 2008). This study uses field data to develop empirical fragility curves for flash flood-induced damage. These curves provide a quantitative relationship between some hazard intensity values and damage degree. Typically, intensity is usually estimated using one, or less commonly two or more spatially distributed parameter(s) describing the destructive capacity of the event (Hungr, 1997). Examples include average velocity, impact pressure, and accumulation height for debris flow. In this study, inundation depth, measured as the mark of height of water flow, is employed as the intensity proxy. Although it may not be the most relevant debris flow intensity descriptor, it is regularly used in empirical studies, since it is directly visible and measurable in the field and easy to interpret by decision-makers.

The paper is organized as follows: Section 1.1 provides an introduction to state of the art in flash flood research, while Section 1.2 summarizes the literature on vulnerability assessment. Section 2 describes the geological and geomorphological settings of the study area, along with details of the rainfall event. Section 3 outlines the methods for rainfall data analysis, debris volume estimation, and vulnerability analysis. Section 4 presents the results, including the application of the developed fragility curves. Finally, Sections 5 and 6 include the discussions and conclusions, respectively.

### 1.1. Some background on flash floods

During a flash flood, sediment-laden water flows in the basin/fan systems are commonly classified as: *i*) debris flows, *ii*) hyperconcentrated flows, *iii*) debris floods, and *iv*) water flows based on their physical properties and the characteristics of a transport mechanism (Van Dine, 1985; Costa, 1988; National Research Council, 1996; Wilford et al., 2004; Pierson, 2005; Santangelo et al., 2012; Borga et al., 2014; Brenna et al., 2021; Brenna et al., 2021).

- **Debris flows** are a highly concentrated mixture of debris and water and can incorporate a wide range of grain size distribution from clay to boulders. They typically contain a sediment concentration exceeding 60 % by volume and are defined as non-Newtonian flows having visco-plastic behavior (Pierson and Costa, 1987; Costa, 1988, Brenna et al., 2021; Brenna et al., 2021).
- **Hyper-concentrated flows** are defined as flows highly charged with fine sediment transported in suspension, typically ranging from 20 % to 60 % by volume. They represent a transition from Newtonian to non-Newtonian fluid behavior, with apparent liquid flow behavior despite containing high amounts of suspended sediment. In rheological terms, hyper-concentrated flows can exhibit plastic to turbulent or laminar behavior (Pierson and Costa, 1987; Costa, 1988; Coussot and Meunier, 1996) in which water transports a high amount of suspended sediment.
- **Debris floods** are rapid flows of water heavily laden with debris in steep channels, causing destabilization of the streambed and massive sediment movement. They commonly occur in mountain streams with abundant coarse sediment supply and steep channels, particularly during intense hydrological events such as flash floods (Brenna et al., 2021; Brenna et al., 2021; Sun et al., 2023).
- **Water flows** involve the movement of clastic particles as suspended load and bedload (Church, 2006; Hicks and Gomez, 2016). Sediment mobilization in water flows is driven by viscous fluid forces acting on individual grains, with suspended sediment concentrations generally below 4 % by volume, maintaining Newtonian fluid behavior (Pierson and Costa, 1987; Costa, 1988, Brenna et al., 2021; Brenna et al., 2021).

### 1.2. Some background on flash flood vulnerability assessment

Vulnerability quantifies the degree of loss in a system exposed to a hazard and is expressed on a scale of 0 (no loss) to 1 (total loss). This addresses the effects of the interaction of a damaging event on the physical environment (Uzielli et al., 2008). One of the most widespread tools in vulnerability analysis is the fragility function, which provides a discrete probability of reaching or exceeding a particular damage level as a function of a hazard intensity measure. Two main approaches are used in vulnerability modeling: *i)* models that describe the degree of loss as a continuous function of hazard intensity, *ii)* models that provide the probability of exceeding discrete damage states (DS) based on intensity measures. The definition of the DS is a part of the model building and depends on some governing factors and degree of observed damage/loss (Papathoma-Köhle et al., 2012; Eidsvig et al., 2014).

The derivation of fragility functions is a well-established research topic in seismic engineering, where building stock is mainly divided into masonry and reinforced concrete. These studies often rely on the EMS-98 damage grades and shaking intensities derived from peak ground acceleration (PGA) estimates (Gautam, 2018; Miano et al., 2020; Gautam et al., 2021). On the contrary, fragility models for hydro-meteorological hazards, such as floods, debris flows and tsunamis are less common. However, there is a growing interest in research focusing on fragility assessments for such events, using parameters such as momentum flux or inundation depth as measures of intensity (e.g. Petrone et al., 2017; De Risi et al., 2019; Gautam et al., 2023). Additionally, urban-scale flood risk assessment methods and applications are increasingly being explored (Zhang et al., 2018; Miranda and Ferreira, 2019 Ferreira and Santos, 2020; Bernardini et al., 2024). Despite this progress, studies addressing vulnerability to flash floods in southern Italy remain scarce, even though the region frequently experiences such events. To bridge this gap, this paper presents a detailed case study of the October 14–15, 2015, rainstorm in the Solopaca–Paupisi area (Benevento province, southern Italy), highlighting its geomorphic effects and associated impacts.

Flash flood-related losses, which can surpass those caused by seismic events, have drawn the attention of insurance and disaster planning entities, emphasizing the need for robust fragility models. The latter frequently utilize field-based intensity measures such as deposition height or inundation depth given the challenges of directly measuring velocity in situ. For example, studies by Fuchs et al. (2007), Fuchs (2008), Akbas et al. (2009), and Papathoma-Köhle et al. (2022) developed vulnerability curves based on damage data from debris flow events in the Italian and Austrian Alps. Similarly, Thapa et al. (2020) created fragility and vulnerability functions for wattle and daub dwellings, brick masonry, and reinforced concrete structures affected by riverine flooding in Nepal (2017), using post-flood depth and damage data. Chen et al. (2021) set up a building damage database made of brick-concrete and masonry-wood in the area affected by the Cutou debris flow (2019) in Wenchuan area, SW China. Using FLO-2D modeling, they proposed

fragility curves based on momentum flux, accounting for flow velocity and depth. Similarly, Gautam et al. (2023) employed momentum flux as an intensity measure in numerical flood fragility models. Losses are typically quantified as monetary values for reconstruction (e.g., Fuchs et al., 2007; Totschnig et al., 2011) or as functional, structural, and aesthetic damages (e.g., Corominas et al., 2005; Lei et al., 2022).

Analytical approaches to fragility modeling, while less common, incorporate detailed physical parameters to simulate the structural behavior of buildings under various loads (Corominas et al., 2014). These methods consider parameter uncertainties, but face limitations related to material behavior, load application, and numerical modeling schemes. For example, Mavrouli and Corominas (2010) and Mavrouli et al. (2014) used finite element models to assess the impacts of rockfalls and landslides on reinforced concrete structures, accounting for uncertainties in frame properties and impacts. Similarly, Quan Luna et al. (2011) combined numerical debris flow modeling with building damage data to develop empirical fragility curves based on debris flow depth, impact pressure, and viscosity. Vulnerability analysis relies heavily on the completeness and representativeness of data. While numerical models and prototype testing provide valuable insights, they cannot fully replicate real-world interactions and outcomes. Empirical data, though subject to biases, directly address these limitations and are indispensable for reliable assessments. Expert-led field investigations are essential to ensure the validity and accuracy of such data.

While there is extensive research on the global vulnerability of structures, fragility functions for nonstructural components remain underexplored. Nonstructural components, being less securely anchored, are more prone to damage from out-of-plane forces and are often more vulnerable to hydro-meteorological hazards, leading to significant loss. This study aims to address these gaps by constructing fragility functions for nonstructural damage based on empirical data collected from a case study in southern Apennines (Italy). In doing so, it contributes to comprehensive vulnerability assessments for flash flood-prone regions.

## 2. Case study

On 14th – 15th October 2015, the Northern Campania Region in Southern Italy was hit by a cloudburst, which triggered debris flows (Fig. 1) and several geomorphological effects on the landscape, resulting in heavy damage to the built environment (Grelle et al., 2019; Guerriero et al., 2020). The effects encompassed areal and linear erosion; with the latter predominantly occurring along the primary channels of the alluvial fans. The dynamics of the event involved an initial phase of deposition marked by lobes reaching heights of up to 1 m, followed by channel erosion and exhumation. Channels experienced significant deepening and widening due to both vertical and lateral erosion, subsequently being filled with deposits from debris flows. Roads played an important role in this process, acting as preferential flow paths and exacerbating the down-cutting of streambeds, which reached depths of 1.5 to 2 m.

The most affected area is Paupisi-Solopaca (Benevento province), located at the foothills of the northern slope of Camposauro mountain as shown in Fig. 1. It represents the southern border of a wide intra-mountain basin that is the Calore River Valley. It covers about 3050 km$^2$ between Telese and Paupisi villages and is located within the axis of the Campanian sector of the Southern Apennines fold-and-thrust belt (Patacca and Scandone, 2007). Its origin occurred in the Plio-Quaternary age due to east-west trending regional faults (Amato et al., 2018).

### 2.1. Geological and geomorphological setting

The geological setting of the study area as shown in Fig. 1 is mainly made of steep Mesozoic carbonate ridges (A) and more gentle Miocene terrigenous flysch slopes (B). On the right bank of the Calore River, five orders of fluvial terraces (C) crop out, while on the left bank, the foot slope area (D) is represented. The latter is made up of three generations of telescopically arranged alluvial fans (mid-late Pleistocene age), where the main urban settlements are located. The Calore River's alluvial plain (Unit E) occupies the central portion of the valley.

The foot slope area is crossed by several tectonic fault scarps mainly N70 and N110 oriented. These scarps represent the surface expression of an active extensional system known as the Calore River fault (Di Bucci et al., 2006). Evidence of active tectonic activity in the region includes the presence of several collapsed sinkholes and mineral springs that are aligned according to the main tectonic directions (Santo et al., 2011; Santo et al., 2019; Corniello et al., 2021). Tectonic processes have also contributed to the disarticulation of the foot slope area and the formation of the telescopic fan systems. As a result, the study area is

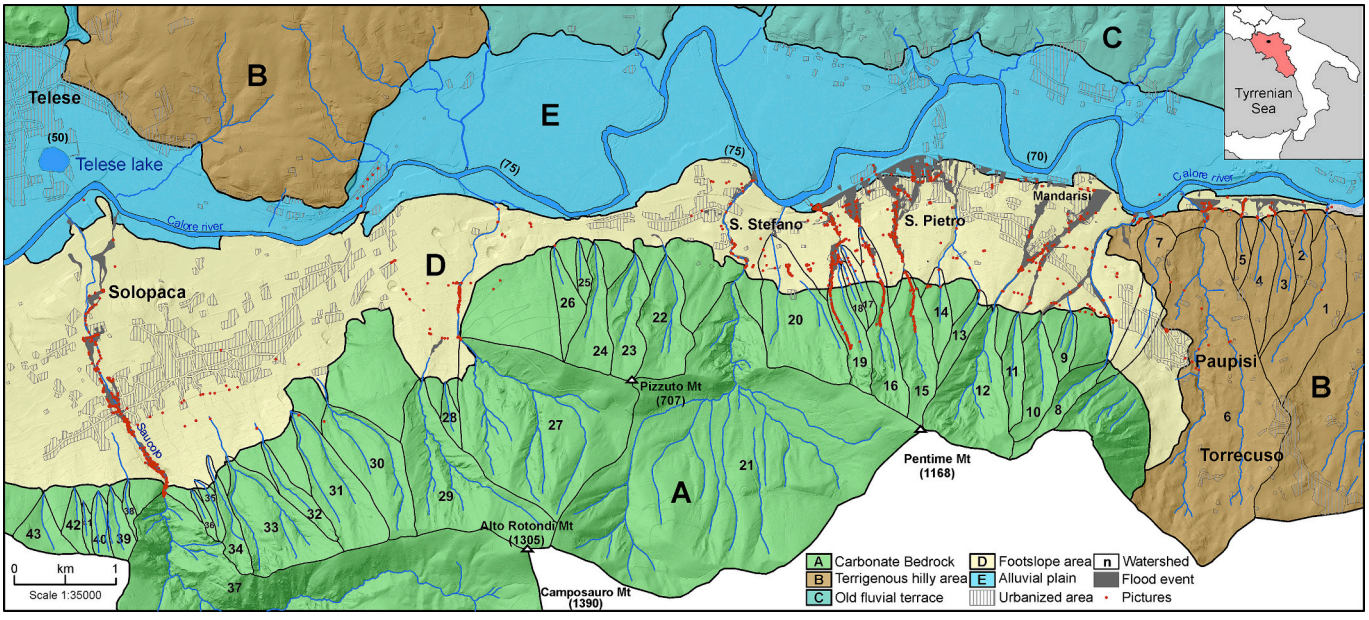


**Fig. 1.** Geological map of the study with the watersheds, flood event, and locations of pictorial evidence (red dots). The numbers represent the ID of the watersheds (see Table 1). (For interpretation of the references to colour in this figure legend, the reader is referred to the web version of this article.)

characterized by both active and inactive (or quiescent) alluvial fans, shaped by a combination of geological, tectonic, and geomorphological processes.

This geomorphological complexity is shown along the 12 km long mountain ridge between Paupisi and Solopaca villages, which hosts 43 basin-fan systems. These systems range in size from less than 0.1 $km^2$ to 8.18 $km^2$ and are sequentially numbered from east to west in Fig. 1, while their main morphometric features are summarized in Table 1. The watershed of the basins is located around 1000 m a.s.l., with a maximum elevation of 1390 m a.s.l. At the foot slope, the basins cross carbonate breccias in pyroclastic matrix with the fan apexes located at 200–300 m a.s.l. (CARG, 2010; Magliulo and Cusano, 2016). Catchments 1–6 rest on flysch bedrock, 7 is both on flysch and limestones, while 8 to 43 are developed exclusively in carbonates. The three catchments (6, 21, and 37) are characterized by a high hierarchical order of the drainage pattern, with deeply incised channel beds having areas between 4 and 8 $km^2$ and concentration times of around 15–30 min. The remaining 40 are small catchments (less than 2 $km^2$) with shallower channel beds and concentration times of less than 15 min. These smaller catchments have ephemeral flow regimes and feed active alluvial fans, some of which are partially covered by settlements.

**Table 1**
Main morphometric parameters of the basin-fan systems.

| N. | BA ($km^2$) | ABS (°) | FCL (km) | FCS (°) | Tc (min) |
|---|---|---|---|---|---|
| 1 | 0.68 | 10 | 1.69 | 10 | 12 |
| 2 | 0.11 | 11 | 0.47 | 11 | 4 |
| 3 | 0.22 | 10 | 0.80 | 10 | 6 |
| 4 | 0.25 | 11 | 0.64 | 11 | 5 |
| 5 | 0.07 | 13 | 0.34 | 13 | 3 |
| 6 | 3.82 | 18 | 3.23 | 18 | 17 |
| 7 | 0.41 | 17 | 1.37 | 17 | 9 |
| 8 | 0.21 | 32 | 0.66 | 32 | 3 |
| 10 | 0.10 | 36 | 0.41 | 36 | 2 |
| 9 | 0.29 | 34 | 0.88 | 34 | 4 |
| 11 | 0.18 | 35 | 0.83 | 35 | 4 |
| 12 | 0.74 | 34 | 1.20 | 34 | 6 |
| 13 | 0.15 | 30 | 0.45 | 30 | 3 |
| 14 | 0.16 | 32 | 0.55 | 31 | 3 |
| 15 | 0.41 | 34 | 1.14 | 34 | 5 |
| 16 | 0.39 | 31 | 1.51 | 31 | 7 |
| 17 | 0.08 | 25 | 0.50 | 25 | 3 |
| 18 | 0.06 | 27 | 0.41 | 27 | 3 |
| 19 | 0.26 | 32 | 0.93 | 32 | 5 |
| 20 | 0.80 | 27 | 1.11 | 27 | 6 |
| 21 | 5.57 | 25 | 3.79 | 25 | 16 |
| 22 | 0.44 | 30 | 0.99 | 30 | 5 |
| 23 | 0.36 | 30 | 0.90 | 30 | 5 |
| 24 | 0.30 | 29 | 0.94 | 29 | 5 |
| 25 | 0.06 | 24 | 0.37 | 24 | 2 |
| 26 | 0.18 | 27 | 0.38 | 27 | 2 |
| 27 | 2.12 | 31 | 2.55 | 31 | 11 |
| 28 | 0.08 | 33 | 0.49 | 33 | 3 |
| 29 | 1.10 | 32 | 2.10 | 32 | 9 |
| 30 | 0.60 | 33 | 1.64 | 33 | 7 |
| 31 | 0.56 | 34 | 1.21 | 34 | 6 |
| 32 | 0.16 | 34 | 0.84 | 34 | 4 |
| 33 | 0.65 | 36 | 1.23 | 36 | 5 |
| 34 | 0.16 | 35 | 0.95 | 35 | 5 |
| 35 | 0.07 | 31 | 0.54 | 31 | 3 |
| 36 | 0.04 | 35 | 0.31 | 35 | 2 |
| 37 | 8.18 | 23 | 6.09 | 23 | 24 |
| 38 | 0.04 | 35 | 0.34 | 35 | 2 |
| 39 | 0.12 | 33 | 0.64 | 33 | 3 |
| 40 | 0.10 | 32 | 0.61 | 32 | 3 |
| 41 | 0.04 | 33 | 0.33 | 33 | 2 |
| 42 | 0.09 | 32 | 0.31 | 32 | 2 |
| 43 | 0.18 | 29 | 0.57 | 29 | 3 |

BA: Basin area; ABS: Average basin slope; FCL: Feeder channel length; FCS: Feeder channel slope; Tc: Time of concentration (Kirpich, 1940).

## 3. Materials and methods

This study is composed of two main parts, each addressing key aspects of flash flood analysis and vulnerability assessment. The first part focuses on analyzing the flash flood event, including a detailed examination of rainfall data, field reconnaissance of geomorphological effects within the basin-fan systems, and volume estimation of mobilized materials. The second one centers on classifying damage to develop fragility curves and applying these curves to assess vulnerability. Together, these approaches provide a comprehensive framework for understanding the physical impacts of the event and advancing methodologies for damage prediction and risk management.

### 3.1. Event characterization

Rainfall data were gathered from 20 rain gauges located within a maximum distance of 30 km from the flooded area. Cumulative rainfall values were calculated at 30-min intervals, along with the total accumulated rainfall recorded at each rain gauge. To depict the spatial rainfall pattern occurred in the most severely affected area during the peak of the extreme event (22:30–01:30), the recorded values were interpolated using the natural neighbor algorithm (NN) in GIS. A cell size of 3 km was selected for the interpolation, based on the average distance of the closest 10 rain gauges considered as most representative of the event. NN is an interpolation technique well-suited for datasets with limited spatial coverage and is known for its reliable performance in such contexts.

The assessment of the magnitude of the flash flood is based on the morphometric description of the geomorphological effects (Hürlimann et al., 2006; Santo et al., 2015), and the data collected after the post-event survey (De Falco et al., 2016; Santo et al., 2016). In particular, the availability of a dataset of 823 aerial photographs in 7 overlapping photo-strips with a ground resolution of 0.5 m from a fixed-wing UAV survey, provided valuable insights for quantifying the event. The campaign covered an area of 13 $km^2$ and was executed at 500 m height with a calibrated digital camera of 14 megapixels. The drone images allowed mapping of the main depositional and erosional processes that were reported at a 1:1000 topographical base derived from a LiDAR with a cell resolution of 1 × 1 m. Furthermore, a traditional field survey was carried out across the reactivated fans from the more distal lobes to the apexes, producing a digital photographic database of nearly 4000 pictures. These were geo-located through Geosetter TM software and GPS waypoints, as shown in Fig. 1 and Fig. 2a. From this collection, 3547 of the most informative pictures were extracted to create a database with the following key attributes:

- Coordinates and optical cone orientation
- Inundation depth (see Fig. 2b)
- Grain size distribution of the deposit, categorized into pebbles ($\varphi >$ 40 cm), gravels (10–40 cm), sand and gravel ($\varphi <$ 10 cm), and mud and silt (see Fig. 2c and Fig. 2d)
- Thickness of the deposited or eroded material (see Fig. 2d, Fig. 2e, and Fig. 2f)
- Damage description (see Fig. 2b and Fig. 2f)

The inundation depth and thickness of erosion/deposition were measured using a metric bar, laser and/or by comparison with scaled objects of known dimensions. As regards the inundation depth, measurements were taken considering the peak flow indicators, such as imprints left on tree trunks and vegetation, or in urban areas, marks left by the flow along the outer walls of buildings or the ones left inside. The estimate of the volume of the sediment transport phenomena could be obtained with two possible approaches: i) by evaluating for each basin the sum of all the eroded areas and their relative thicknesses and ii) by calculating the sum of volumes deposited in the fan area. The second approach was preferred over the first, as it would have been difficult to

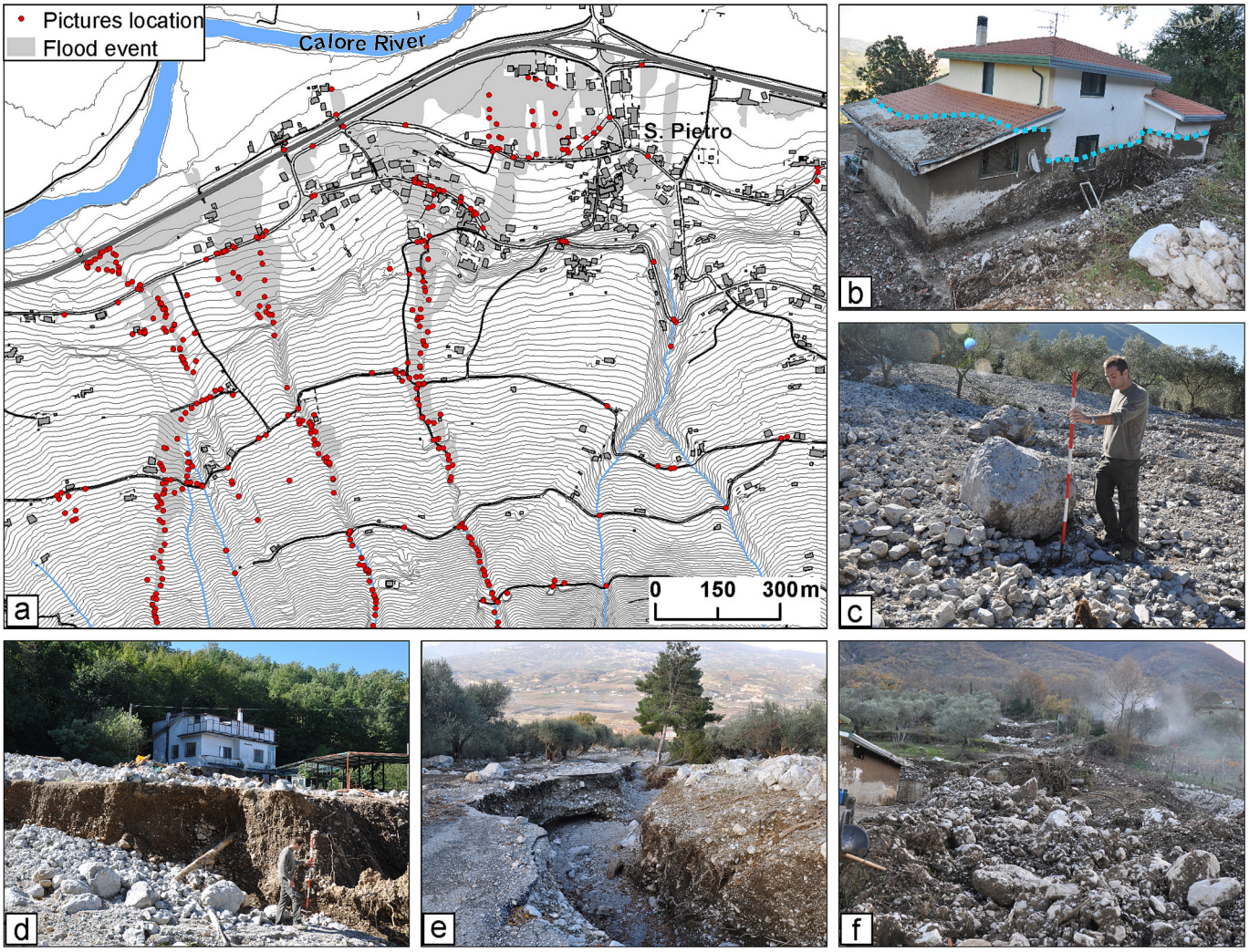


**Fig. 2.** Collected field data: a) distribution of the geotagged pictures and flood event mapping, b) example of inundation depth measurement and damage recording, c) identification of grain size of the deposit, d) assessment of grain-size and thickness of erosion and deposition, e) example of erosion area, f) example of deposition area.

evaluate the erosion in the mountainous areas with gullies that are narrow, steep, and often not easily accessible. However, the methodology adopted has some limitations as it does not account for a considerable amount of small particle material. Some of which reached the Calore River (basin no. 21), and some got locally deposited within the mountainous areas of the watershed. Therefore, the estimated volume of mobilized material should be considered an underestimate of the true value. The volume ($V$) of deposited material was estimated for each reactivated watershed using the following equation:

$$V = (FA - EA) \times t \quad (1)$$

where $FA$ is the footprint area of the flood event in a given watershed, where the reactivated lobes are located; $EA$ is the erosion area represented by channels and gullies within the footprint of FA, which was derived from the post-event drone survey; and $t$ is the thickness of the deposits extracted from the thickness map.

The thickness map was obtained using Geospatial Analyst in ArcGIS®, which provides several deterministic and geostatistical interpolation techniques. Deterministic interpolation methods create surfaces from measured points, based on either the extent of similarity such as the Inverse Distance Weighted (IDW) or the degree of smoothing such as Radial Basis Functions (RBF). In this study, several deterministic interpolation techniques, including IDW, Local Polynomial Interpolation (LPI), Global Polynomial interpolation (GPL), and RBF were used to generate the spatial distribution of deposit thickness. Since RBF method is a group of five deterministic interpolation techniques: thin-plate spline (TPS), spline with tension (SPT), completely regularized spline (CRS), multi-quadratic function (MQ), and inverse multi-quadratic function (IMQ), the choice was made considering the best performance among them. The evaluation of the accuracy of interpolation was done using the cross-validation method, namely the leave-one-out technique. This involves omitting a single sample value from the entire dataset and performing interpolation procedure using the remaining dataset and then calculating the difference between the actual and predicted value for the omitted point. This procedure is repeated for n times, where n is the number of samples. Finally, the best interpolation method was selected two of the most common statistical metrics: ME (Mean Error) and RMSE (Root Mean Squared Error).

### 3.2. Damage assessment and fragility curves

Damage to the built environment involved both environmental losses and damage to the building stocks. In the first case, the damage occurred on cultivations (mainly olive groves and vineyards). In terms of infrastructures (roads, pipelines, electric lines) damage occurred due to several natural phenomena such as erosion and deposition caused by

rills, gullies, and small landsliding as described and mapped by Santo et al. (2016). The flow mainly moved parallel to the former channels, in a few cases breaching the outside walls of houses. Doors, windows, stores, and fences were commonly damaged, together with flooding of the ground floors, basements, gardens and yards. In contrast, the deposition of coarse materials, such as pebbles and gravel, along with soil erosion, caused more significant damage, particularly to agriculture. This damage strongly impacted on the local economy, which relies heavily on agriculture and wine production. However, this paper focuses specifically on the damage to building stocks.

The damage description follows the classification scheme proposed by Diakakis et al. (2020). The authors proposed a severity scale based on 10-degree of impact divided into four categories of affected elements. These are: *i)* impacts on the built environment (including any human-built structure, property or infrastructure, excluding mobile objects), *ii)* impacts on man-made mobile objects, including vehicles, household items, and other objects, *iii)* impacts on the natural environment, including vegetation and agricultural fauna, pollution phenomena, geomorphic effects, and *iv)* impacts on the human population, including emergency evacuations, entrapments, individuals who received rescue, injuries, and fatalities. This study focuses on the first category, which ranges from 'Class I' (simple road inundation and yard or garden flooding with no structural damage) to 'Class X' (where large dams collapse due to the flash flood). For this event, the original damage classes were merged to identify damage states (DS) as reported and described in Table 2 and shown in Fig. 3. The highest damage state observed was DS3, corresponding to Class V.

**Table 2**
Impact on the built environment ranked in classes of progressive severity along with description and the associated DS (modified from: Diakakis et al., 2020).

| Class | Description | DS |
|---|---|---|
| I | Yards/Gardens suffer inundation on individual buildings. Inundation occurs of road or sidewalk surface. Low water crossings are flooded. No structural damage appears on any infrastructure or individual buildings. | 1 |
| II | Flooding is limited to basements. Only ground-based equipment and furniture affected. Underground passage/traffic lights out of order. Culverts and sewerage network affected or blocked. No structural damage appears on any infrastructure or individual buildings. | |
| III | Ground floors suffer flooding affecting only ground-based household furniture or equipment or floors and floor tiles. Absorbed moisture on walls. Basement flooding affects higher positioned equipment or furniture, central heating unit, and relevant equipment/boiler. Roads not passable due to inundation. Terminal stations flooded. No structural damage appears on any infrastructure or individual buildings. | 2 |
| IV | Ground floor flooding affects higher positioned equipment or furniture. Yard walls and fences suffer structural damage. Traffic lights and road signage suffer damage. Single span bridges inundate. Railway lines are not passable due to inundation or debris. Bridges suffer damages at railing installations, Telecommunication networks interrupted/power lines | 3 |
| V | Damages on wall coverings/plaster/veneer/false ceilings and walls, Garage doors, window frames and floor tiles/1st floors suffer flooding. Roads suffer damages due to asphalt surface or foundations scouring/ Levees scoured/Artificial, reinforced concrete (RC) riverbanks suffer damages/Water and sewerage mains break | |
| VI | Structural damage visible, subsidence or deformation of building elements. Roads together with their foundation suffer complete destruction/Small footbridges collapse/Rail lines suffer damages/ Levees break | – |
| VII | Partial structural damage of the building, deformation of supporting elements/Buildings made of wood or stone collapse | – |
| VIII | Complete collapse of RC or metal buildings. Single-span bridges suffer complete collapse/Damages in RC constructions of ports, docks/ Partial damages in elements of large buildings (e.g. industrial), power plants, refineries, nuclear plants/multi-span bridges suffer partial collapses. | – |
| IX | Large buildings (e.g. industrial) observe complete collapse. Multi-span bridges suffer complete collapses. | – |
| X | Large dams break/Significant parts of large power plants, refineries, nuclear plants suffer complete collapse. | – |

The damage data was then used for the construction of fragility curves based on the damage states modified from the original damage classification system proposed by Diakakis et al. (2020) and the inundation depth recorded from the observation data. The dataset was divided into training (97) and testing data (33); the latter is made of the damaged buildings in the fan area of the largest basin (no. 37) at Solopaca village. Lognormal function is chosen to construct the fragility functions fitting the depth and damage data calibrating separately three relations for each damage state (DS1, DS2, and DS3) using the observations falling in each class. Lognormal distribution is chosen due to its convergence at zero and negative intensity measure value, which is not the same in many other distributions. It is worth noting that several researchers have considered various statistical distributions (e.g. Parisi and Sabella, 2017; Gautam, 2018) such Weibull, linear, logistic function, n-order polynomial, among others to depict vulnerability. The functional form of the lognormal fragility function is given as:

$$P(DSi|IM = x) = \Phi\left(\frac{ln\left(\frac{x}{\theta}\right)}{\beta}\right) \tag{2}$$

where $P(DSi|IM = x)$ is the probability that an intensity measure (IM) of the considered hazard (inundation depth) with $IM = x$ will cause the $i^{th}$ damage state ($DSi$); $\Phi$ is the standard normal cumulative distribution function (CDF), $\theta$ is the expectation (i.e. the $IM$ level with 50 % exceedance probability), and $\beta$ is the standard deviation of $ln(IM)$. Eq. (2) implies that the $IM$ values of flow height causing a certain $DS$ are lognormally distributed, which is a most common assumption in vulnerability studies. Calibrating Eq. (2) requires estimation of $\theta$ and $\beta$. In this case, the randomness is due to record-to-record variability, as the same $IM$ level produces different demands on a given structure. The maximum likelihood method is adopted for parameter estimation.

Despite the median distribution parameters, the epistemic uncertainties arising due to limited data are also desirable. Uncertainties are incorporated by the 95 % confidence bounds for each parameter. The confidence intervals (CI) for the lognormal mean with $n-1$ degrees of freedom can be estimated as follows (Crow et al., 1960):

$$CI_\theta = ln(\theta) \pm t_{\frac{\alpha}{2},n-1}\frac{\beta}{\sqrt{n}} \tag{3}$$

where $t_{\frac{\alpha}{2},n-1}$ indicates the t-distribution value for $n-1$ degrees of freedom and $\alpha$ is taken as 0.05. The 95 % confidence interval values for the dispersion parameters are estimated as:

$$CI_\beta = \sqrt{\frac{(n-1)\beta^2}{\chi^2_{\frac{\alpha}{2},n-1}}}, \sqrt{\frac{(n-1)\beta^2}{\chi^2_{1-\frac{\alpha}{2},n-1}}} \tag{4}$$

Two sets of fragility functions are developed for each damage state considering uncertainties only in the central tendency parameter keeping the dispersion parameter constant and considering uncertainties in both central tendency and dispersion parameters. Finally, fragility functions are used in flash flood vulnerability assessment for the buildings affected by the flood that occurred in basin no. 37, and the resulting maps are juxtaposed with the actual damage.

## 4. Results

### 4.1. Rainfall characterization and flash flood intensity assessment

The cloudburst event began on 14 October 2015 around 21:00 and ended at about 04:00 the next day (15 October). Rain gauges closer to the most affected area recorded rainfall values of about 150–250 mm in 7 h, with the maximum of around 140 mm within 2 h (De Falco et al.,

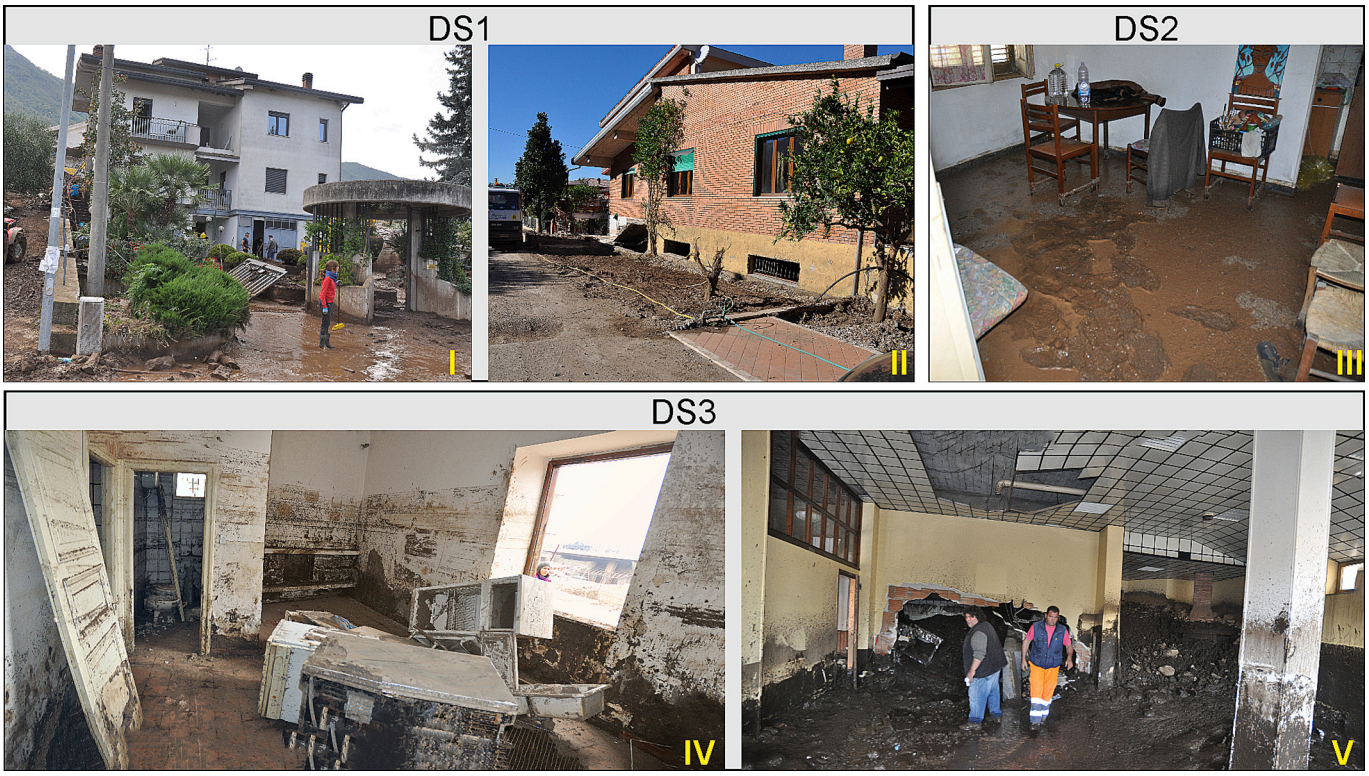


**Fig. 3.** Classification of the damage states (DS) identified in field as per the classification system proposed by Diakakis et al. (2020).

2016; Santo et al., 2016). The highest rainfall value was found for the Paupisi rain gauge (no. 7) that recorded a total of 400 mm rainfall for the whole event. In the neighboring areas, a dense network of rain gauges was in place, and data from 20 gauges within a 30 km radius were collected, as shown in the inset of Fig. 4. This data was used to analyze the rainfall pattern by interpolating the cumulative rainfall and the

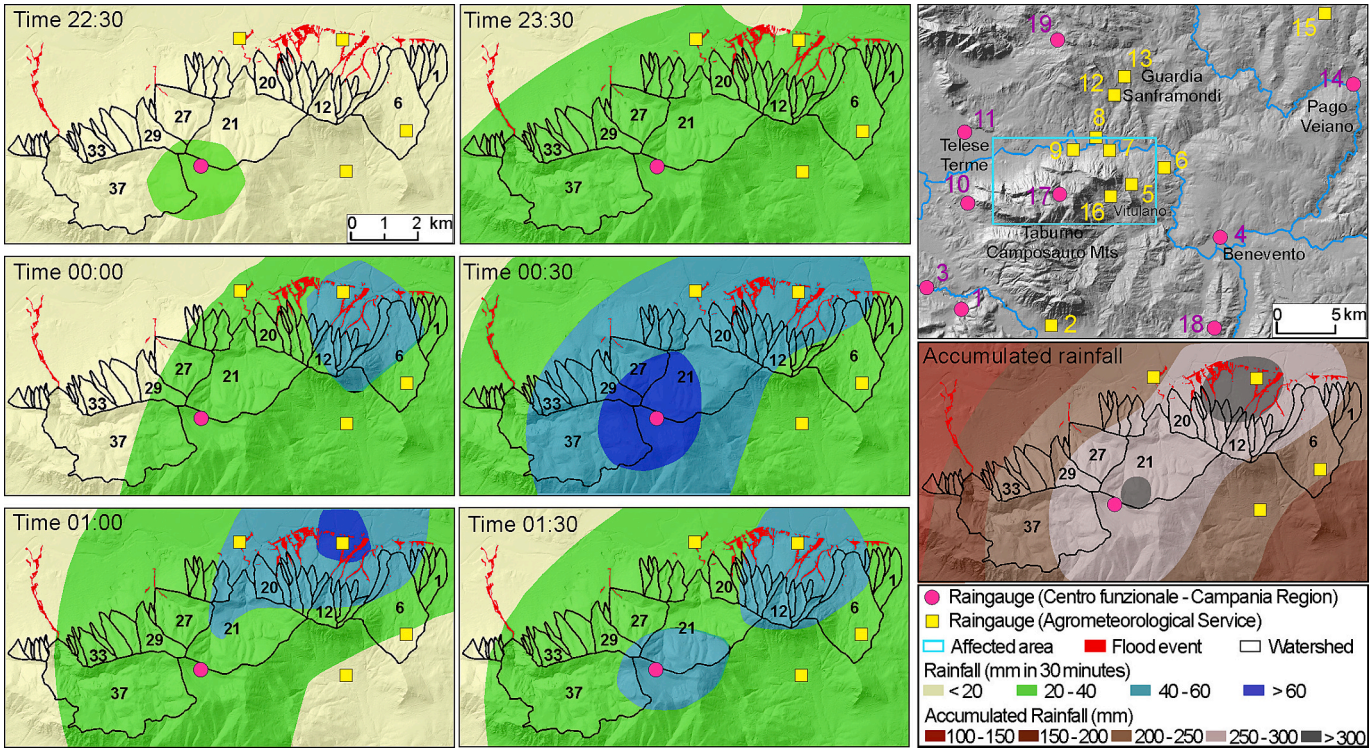


**Fig. 4.** Distribution of rain gauges, illustration of rainfall intensity variation every 30 min for the whole duration of the flash flood, and accumulated rainfall map. Rain gauges: 1) Sant'Agata dei Goti; 2) Airola; 3) Sant'Agata dei Goti Isclero; 4) Benevento; 5) Torrecuso-507; 6) Torrecuso-172; 7) Paupisi; 8) San Lorenzo Maggiore; 9) Vitulano-96; 10) Melizzano; 11) Sorgenti Grassano; 12) San Lupo; 13) Casalduni; 14) Pago Veiano; 15) San Marco dei Cavoti; 16) Vitulano; 17) Vitulano-Camposauro; 18) S. Leucio del Sannio; 19) Cerreto Sannita.

amount every 30 min from 22:30 to 01:30 as shown in Fig. 4.

The rainfall maps show that the event started at 22:30, with 20–40 mm (in 30 min) at the top of Camposauro mountain, gradually spreading across the area over the next hour. Afterward, the intensity became higher (40–60 mm) and moved north-eastward, where the cloudburst mainly occurred on the catchments crossing the Paupisi town until 01:30. The highest rainfall value in 30 min occurred at around 00:30 at the top of the basins 21–27–29-37 that produced debris flows in Solopaca town and at around 01:00 it passed through Paupisi catchments. It is possible to observe an overlap between the traces of sediment deliveries and the localization of the higher rainfall intensities, which is also highlighted by the cumulative rainfall map where these pieces of evidence are characterized by values higher than 250 mm. Conversely, several small watersheds (28 to 36 and 38 to 43) did not show field evidence of debris movement in the foot slope area.

The approach outlined in Section 3.1 was used to estimate the volume of deposited material and represent the flood event for each basin/fan system. Fig. 5a reports the watersheds of the whole study area colored as a function of the estimated deposition volume for each basin. The estimation is variable, the highest (more than 30.000 $m^3$) can be observed at the largest watershed (no. 37), and also for two smaller basins (no. 11 and no. 15) in which the rainfall was intense (more than 50 mm in 30 min) for two hours and the accumulated rainfall reached 250–300 mm. The other six basins were characterized by volumes spanning from 30.000 to 15.000 $m^3$.

Fig. 5b shows a thematization of thickness deposits derived from the interpolation of point data extracted from 4000 pictures collected in the field and elaborated as detailed in Section 3. In total, 3547 datasets were

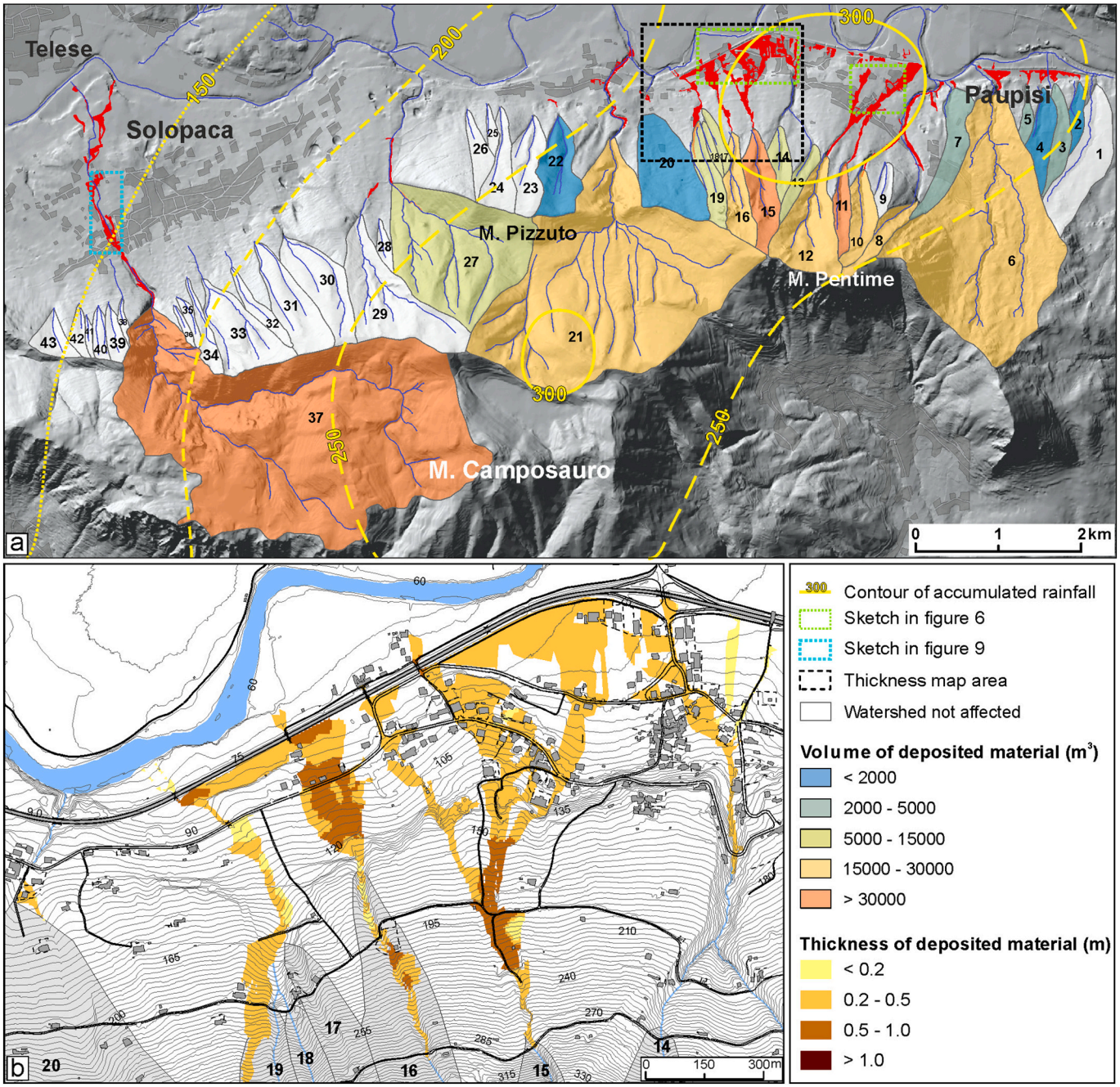


**Fig. 5.** a) Distribution of the estimated volumes of deposited material for each watershed, the values of the volumes refer to the red colored areas, b) deposit thickness distribution. (For interpretation of the references to colour in this figure legend, the reader is referred to the web version of this article.)

processed using raster interpolation technique. Afterward, the cross-validation, ME, and RMSE were calculated. Table 3 presents the summary of the metrics for different interpolation methods. It shows the lowest values of ME and RMSE for RBF (multi-quadratic function) method.

The interpolated map is reported in Fig. 5b. The thickness of the deposited material is usually between 20 and 50 cm; higher values can be found in basins n. 15, 16, and 37. In the flanks of the main channels and especially in the distal fans, the thickness of the accumulated material is around 20–50 cm, which increases when the flow finds obstacles perpendicular to its direction such as road embankments, yards, and concrete walls. Field surveys showed how the local morphology influenced the deposition phase. In some cases, the local deposition phenomenon occurred in accordance with the terraces for agricultural use or roads normal to the flow.

### 4.2. Flood vulnerability and example application in Solopaca (watershed no. 37)

The identification of the damage to the building stock permitted us to collect 130 records, of which some significant examples are reported in Fig. 6. Notably, 130 is one of the greatest amount of data when compared to the existing studies.

The most common class is represented by nonstructural damage, i.e. I, II and III with the flooding of ground floors, whereas IV and V classes corresponding to the failure of walls of yards and fences in RC buildings are rare. Although the higher damage classes (IV and V) affected RC buildings, the variation in the construction system (RC or masonry) is neglected as neither of such classes observed structural or global damage. These data were processed to construct vulnerability curves for the three damage states (DS) that are converted from damage classes defined in Table 2. The dataset highlights that the degree of damage DS increases with inundation depth, which is as expected. In fact, the median inundation depth is 30 cm for DS1, 50 cm for DS2, and to 80 cm for DS3 as shown in Fig. 7a. Fig. 7b shows the distribution of the inundation depth for the DS, in particular, DS1 is characterized by values lower than 60 cm, with the highest frequency in the range of 20–30 cm, DS2 starts at 20–30 cm and reaches values greater than 80 cm, while DS3 is in the range 40 cm to greater than 80 cm. The fragility curves based on lognormal likelihood are shown in Fig. 8. Among the 97 data of the training set, 62, 26, and 9 data were attributed respectively to DS1, DS2, and DS3. The lognormal distribution parameters and their uncertainties for each damage state are reported in Table 4. Table 4 and Fig. 8 collectively highlight that the uncertainties are greater in higher damage states. This is because of the limited amount of data attributed to the higher damage states. Since lower damage states pertain to well distributed and greater amount of data, uncertainties are lower in lower damage states. It is important to note that the uncertainties addressed in Table 4 are the only epistemic uncertainties; however, aleatoric uncertainties arising due to the variation in the physical attributes of affected structures would play a pivotal role in the extent of damage. Furthermore, while interpreting fragility functions and their uncertainties, one should keep in mind that the inundation depth alone is not the explicit intensity measure, but rather momentum flux and its duration are equally important or even more representative to characterize damage. Meanwhile, the major challenge behind the use of momentum flux and duration is that one cannot precisely measure the flow velocity and the duration of the characteristic velocity. In this case, the only plausible intensity measure becomes the inundation depth.

**Table 3**
Performance metrics for deterministic interpolation methods.

| Metrics | Formula | Deterministic method | | | |
|---|---|---|---|---|---|
| | | IDW | GPL | RBF (MQ) | LPI |
| ME | $ME = \frac{1}{n}\sum_{i=1}^{n}(\hat{y}_i - y_i)$ | 0.00406 | 0.00239 | 0.001850 | 0.00341 |
| RMSE | $RMSE = \sqrt{\sum_{i=1}^{N}\frac{(\hat{y}_i - y_i)^2}{n}}$ | 0.09151 | 0.22533 | 0.081296 | 0.13299 |

$\hat{y}_i$is the measured value; $y_i$ is the estimated value at the sampling points $I$ ($i$ = 1,2, …, $n$), and $n$ is the number of values used for the estimation.

The fragility curves highlight that at an inundation depth of 50 cm, the probabilities of exceeding the DS1, DS2, and DS3 are respectively 96 %, 59 %, and 11 %. Conversely, the 50 % probability to overcome the DS3 is attained at 75 cm, while nearly 90 % exceedance probability is attained at more than 1 m (1.15 m), which is still below the story height. This indicates that there is strong likelihood of significant loss due to a flood event that can lead to an inundation depth of 1.15 m. At 1.15 m inundation, people cannot use the facility anymore. Thus, the indirect losses and functionality losses are greater than the actual physical losses. However, indirect losses such as functionality loss require due attention, and unique details should be studied separately. After 1.6 m inundation, all the curves saturate, which is the indication of the occurrence of higher damage states. However, due to the lack of sufficient data, this study cannot envisage such curves.

The fragility functions were finally used to develop three vulnerability maps for the case study area, i.e. Solopaca (basin no. 37). Each curve pertaining to a unique damage state is used to draw a scenario map depicting the probability of exceeding/reaching each damage state. Hatched representation in Fig. 9 is used to represent the damage state of the field evidence reported in the testing dataset (33 data). For DS1, nearly all the buildings have a very high probability (> 75 %) of reaching/exceeding DS1 as it is represented by simple flooding of gardens, basements or ground floors, which require minimal recovery/repair cost. A comparison with the attributed DS significantly adheres to the flooding scenario. The buildings characterized by higher damage states are those located along the main flow direction. DS2 encompasses the flooding of ground floors affecting ground-based household furniture and basement flooding affecting higher positioned equipment or furniture. In this context, a trend of decrease in probability with the increase of distance from the hydrographic apex along the flow direction can be observed. DS3 affects higher positioned equipment or furniture, yard walls and fences, cracks on wall coverings and garage doors, window frames, and 1st floors flooding, etc. This scenario is characterized by a lower probability that is mainly represented by less than 25 %. Also, in this case, the highest vulnerability can be found for the buildings closer to the hydrographic apex, as confirmed by the attributed DS too.

## 5. Discussions

### 5.1. Reconstruction of flash flood scenario

The field survey data allowed us to make some notable considerations on the event occurred in the Paupisi-Solopaca area that can be useful to better define the flooding scenario in similar geomorphological settings and can also provide insights into flash floods resilience planning.

First, the intensity of the flash flood event was evaluated by means of the evaluation of the volumes of materials deposited in the fan area ranging between 30.000 and 15.000 $m^3$ It can be outlined that the volumes of materials deposited in the fan area seem to be correlated with the rainfall intensity distribution and the cumulative value other than the size of the feeding catchments. In fact, they significantly differ in size: the highest volumes (more than 30.000 $m^3$) can be observed for the largest watershed (no. 37) but also for two smaller catchments (no. 11 and no. 15), while six basins of variable extent were characterized by volumes spanning from 30.000 to 15.000 $m^3$. It is also important to highlight that closer basin had significantly different geomorphic

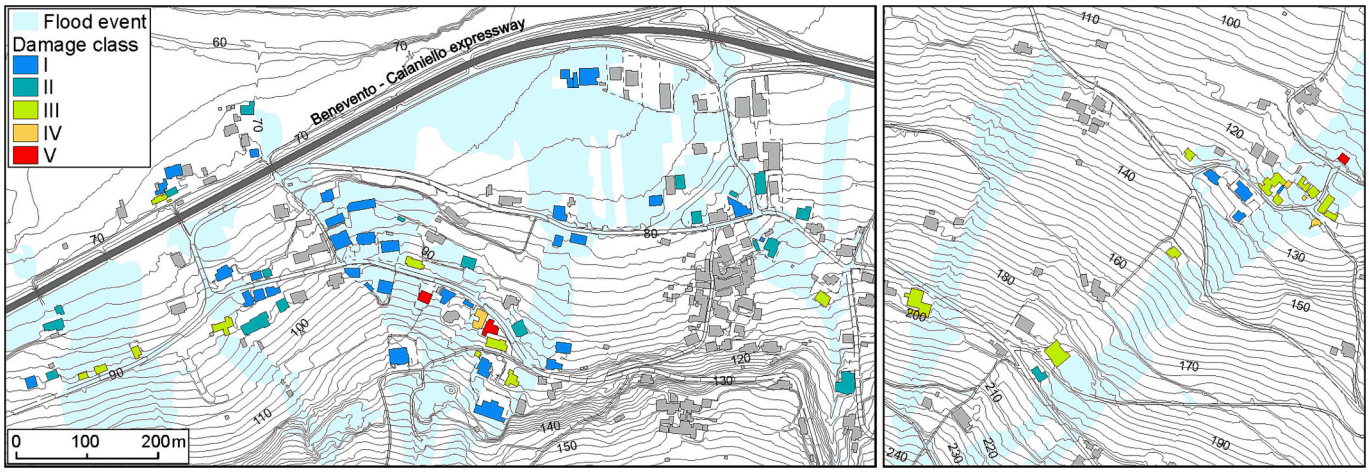


**Fig. 6.** Damage distribution in the most affected areas following Diakakis et al. (2020) classification scheme. Refer Fig. 5 for the location reference.

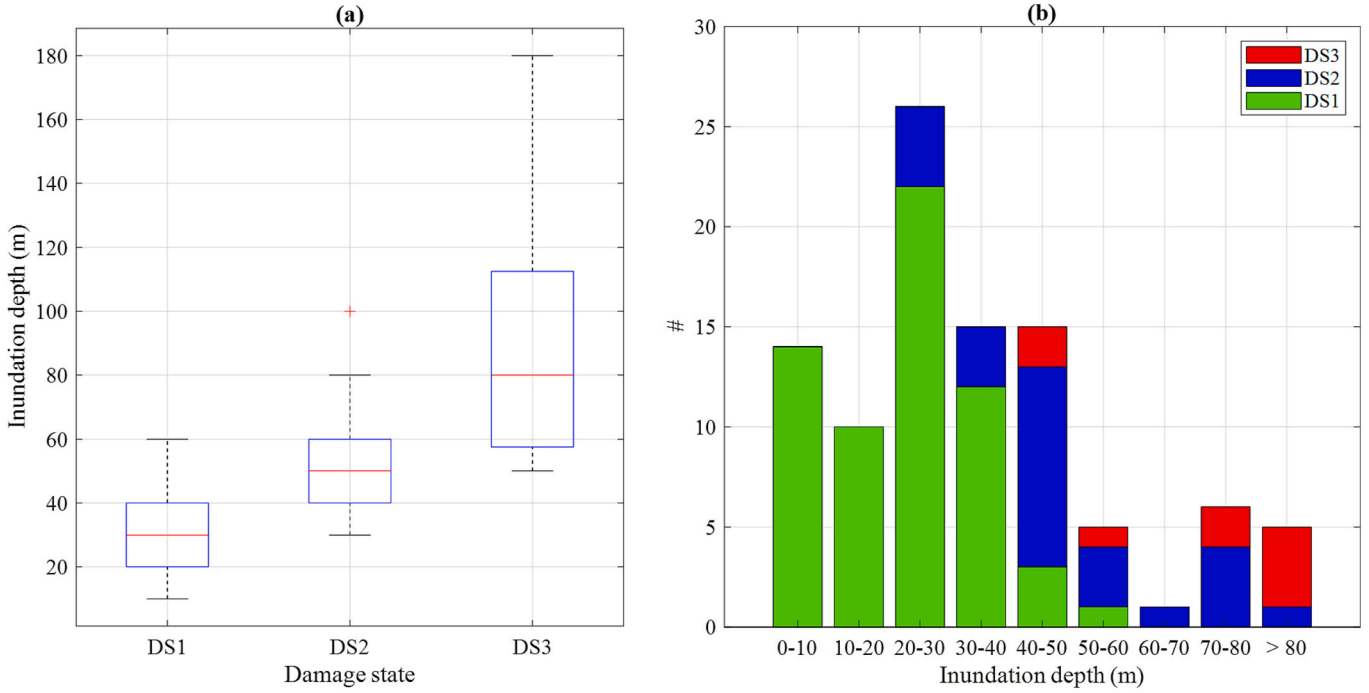


**Fig. 7.** a) Boxplot of the inundation depth for each damage state, b) frequency distribution of damage states pertaining to inundation depth ranges.

responses, in fact many of them were not activated at all. Even if other significant factors such as the sediment budget of each basin have to be taken into account (Palumbo et al., 2024), this evidence can be explained also by referring to the rainfall intensities reported in Fig. 4. There is in fact a correspondence between the activation of debris flow traces and the localization of the higher rainfall values. Furthermore, the cloudburst clearly moved from SW to NE involving only some of the watersheds of Camposauro mountain, the others were not affected by rainfall intensities greater than 40 mm in 30 min as in the case of basin no. 43 to 38. Conversely, other small watersheds such as no. 36 to 28 were protected by the extent and shape of the largest basin (no. 37), which collected most of the rainfall and mobilized more than 30.000 $m^3$ of debris and mud affecting Solopaca village with subsequent damages. The rainfall event lasted for 7 h, with a maximum of around 140 mm within 2 h. It represents a typical pattern of high intensity and short duration rainfall in the Apennines, where the effects on the ground can also be very different in neighboring areas, causing a notable debris movement in small catchments.

The data collected during the post-event field survey (inundation depth, deposit thickness, and grains size) are strictly connected with the damage occurred during the flash flood. The most frequent classes are 0.5–1 m for the inundation depth, and 20–50 cm for the thickness of the deposits. Gravels are the predominant grain size, although several other classes are overlaid due the fact that the surveyed thickness is the result of progressive aggradation phenomenon. The collected data also showed that the flow had the capacity to transport parked cars and trees, but the presence of anthropic elements (walls, fences, roads, buildings, terraces) strongly influenced flow propagation and sediment deposition, suggesting that an effective prevention plan must also take these elements into account.

### 5.2. *Application and comparison of vulnerability curves*

A key contribution of this study, in terms of vulnerability analysis, is the development of fragility curves that define damage states, adapted from the original damage classification proposed by Diakakis et al.

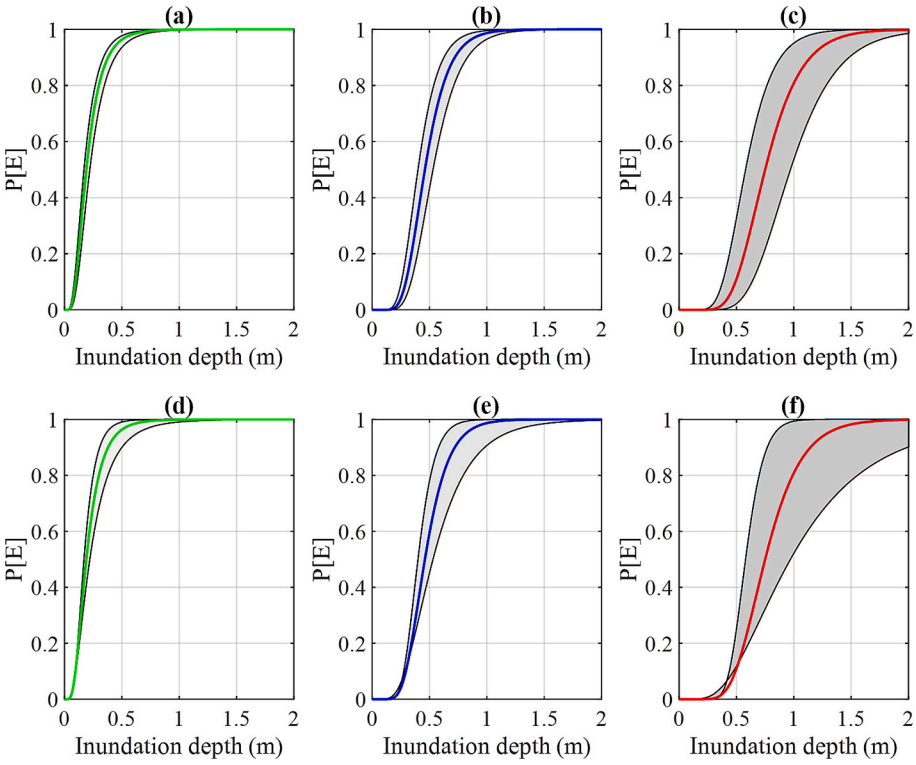


**Fig. 8.** Flash flood fragility functions for nonstructural elements: a), b), and c) indicate median fragility and uncertainty respectively for DS1, DS2, and DS3 considering uncertainty only in median parameter; d), e), and f) depict the same considering uncertainties in both median and logarithmic standard deviation.

**Table 4**
Lognormal distribution parameters and their uncertainty bounds.

| Damage state | Lognormal distribution parameters | | | | | | # of samples |
|---|---|---|---|---|---|---|---|
| | Median | | Upper 95 % bound | | Lower 5 % bound | | |
| | $\theta$ | $\beta$ | $\theta$ | $\beta$ | $\theta$ | $\beta$ | |
| DS1 | 0.19 | 0.54 | 0.22 | 0.64 | 0.17 | 0.46 | 62 |
| DS2 | 0.46 | 0.35 | 0.53 | 0.48 | 0.40 | 0.29 | 26 |
| DS3 | 0.75 | 0.33 | 0.97 | 0.56 | 0.58 | 0.22 | 9 |

(2020). Specifically, vulnerability functions were derived exclusively for buildings, while damage to agricultural activities, rural roads, and some infrastructure—although significant—was not considered. In many instances, the electricity distribution network, telecommunication infrastructure, gas lines, as well as the aqueduct and sewage systems, were also damaged. Additionally, small bridges and underpasses were eroded or destroyed by alluvial process. The application of these curves in one of the basins (no. 37 at Solopaca village) used as test area resulted in a good fit with the maps shown in Fig. 10 with the highest vulnerability values found for the buildings closer to the hydrographic apex. DS3 occurrence is limited to 1 km from the hydrographic apex, DS2 can be observed until a maximum distance of 1400 m, while DS1 is recognized at both close and far distances, as it is strongly influenced by local urban footprint. The median fragility curves derived in this study for the DS1, DS2, and DS3 are compared with the vulnerability curves proposed by other researchers for similar phenomenon such as the ones proposed by Fuchs et al. (2007), Akbas et al. (2009), and Papathoma-Köhle et al. (2012) as shown in Fig. 10. Although the curves do not necessarily represent the same flooding scenarios and built environments, the general perception is that the southern Apennines building stocks are likely to observe nonstructural damage at lower inundation depth than the rest of the building stocks reported in the literature.

The vulnerability curves existing in literature are derived using different mathematical approaches and distributions calibrated on flood events characterized by debris flows originated from alpine catchments. They are characterized by different trends although inundation depth values are quite similar. Akbas et al. (2009) derived fragility curves from numerical analyses through back calculation of the Selvetta debris flow that occurred on 13 July 2008 in Valtellina (Northern Italy). Fuchs et al. (2007) derived vulnerability curves using damage data from the debris flow event in the Wartschenbach catchment in the eastern Alps, next to the city of Lienz, Austria. Papathoma-Köhle et al. (2012) developed their study from a very high magnitude event caused by the dam break due to the overflow of the reservoir after the opening of flood gates in Martell Valley (Süd Tyrol) in August 1987. The damage assumed in these studies is representative of structural failure conditions due to debris flow impact for buildings in northern Italy and Austria. Conversely, in this study the fragility curves essentially report the lower damage states only as the structural failure of buildings was never attained. In this regard, the proposed fragility curves could serve as a tool for nonstructural flood vulnerability analysis. The comparison shown in Fig. 10 highlights that Southern Apennine constructions are more vulnerable until damage is limited to nonstructural elements. This conclusion is made on the assumption that the vulnerability models proposed in the existing literature comprise a mixed damage scenario, i.e. damage to both nonstructural and structural elements. In this case, the more vulnerable nonstructural elements will damage before any structural element observes damage. In this case, all three vulnerability models adhere to DS3 of this study at lower inundation depth, surpassing DS1 and DS2. Even for DS3, the proposed curve immediately saturates at around 2 m, whereas the existing curves start to saturate only after 2.5 m inundation. However, one should note that the existing vulnerability models do not solely represent nonstructural damage, but an ensemble of both structural and nonstructural damage. Apparently, 100 % exceedance probability of DS3 is attained even if a flood equivalent to one full story height ($\sim$ 3 m) does not occur. This indicates that nonstructural elements are highly vulnerable to flash floods. Although the overall damage extent is limited, functionality loss is always prominent and so is economic

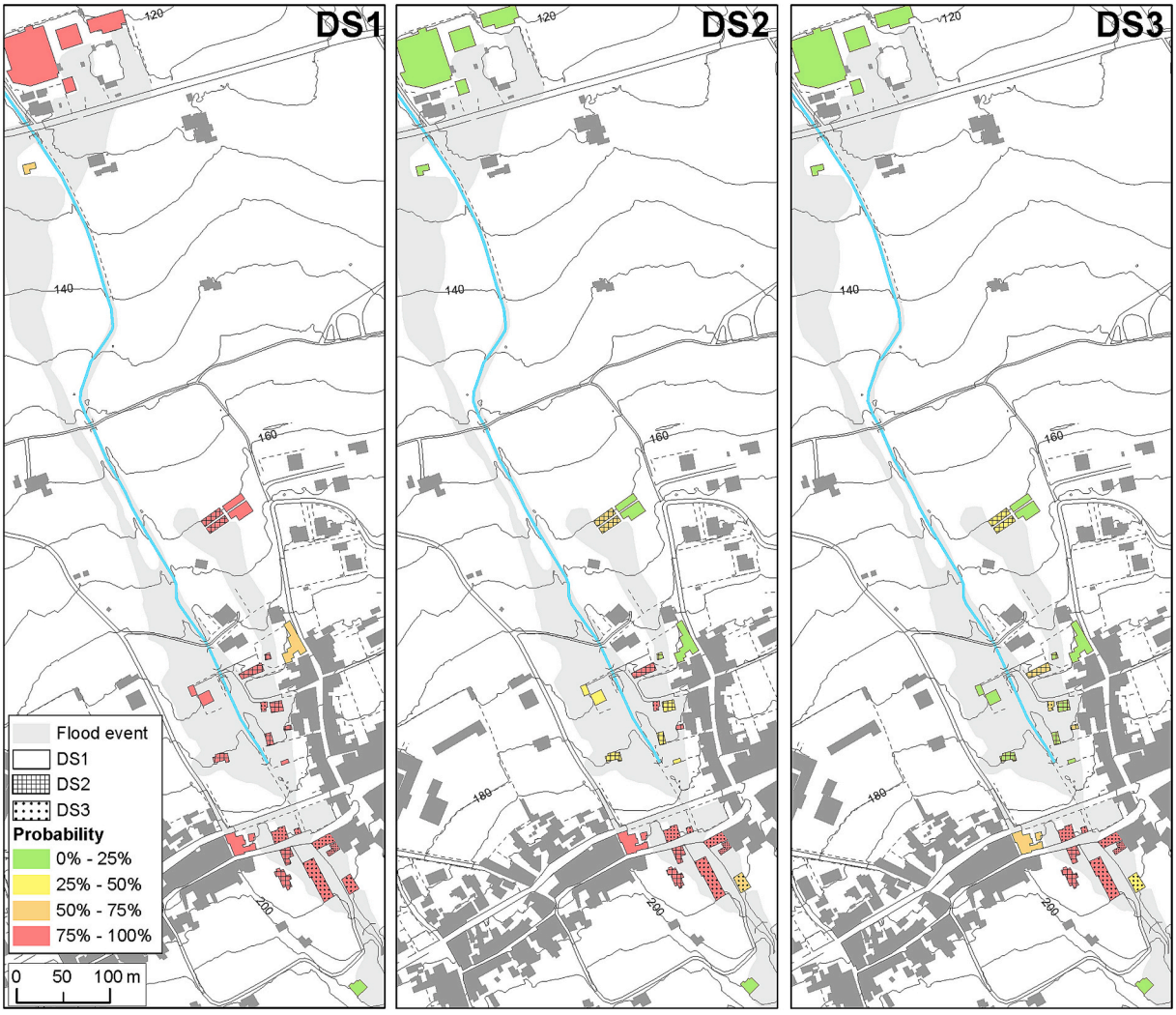


**Fig. 9.** Vulnerability scenario mapping for Solopaca village (refer Fig. 5 for the location).

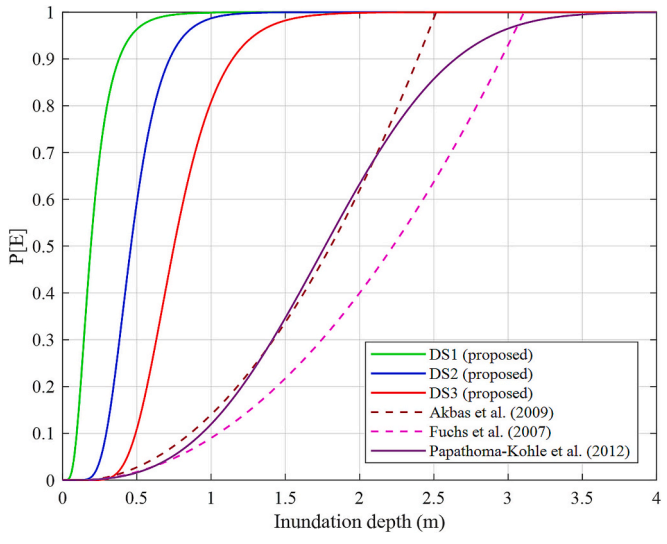


**Fig. 10.** Comparison between the fragility curves developed in this study with existing vulnerability curves from literature.

consequence even when nonstructural elements are damaged. Thus, quantification of nonstructural damage is ideally important even though flooding extent is not detrimental. Due to similarity in nonstructural element construction in many parts worldwide, the fragility models could be used for benchmarking purposes as well. Fragility functions depict discrete information regarding the damage occurrence, so they provide more rational information for decision making and pre-event planning. Also, future insurance premium planning and possible considerations for flood mitigation measures could benefit from the proposed fragility functions. For practical applications such as in insurance premium planning and flash flood preparedness and prevention initiatives, fragility functions considering uncertainties in both lognormal parameters are recommended. The uncertainty bounds can be used for expert elicitation/judgment for practical applications to decision-making. Based on the criticality of the built-environment or physical asset, fragility functions can be chosen from the two sets.

## 6. Conclusions

This study highlights the challenges posed by flash floods in the Apennine region, where watersheds are characterized by small spatial extent (less than 10 $km^2$) and steep slopes (greater than 30°). Such watersheds can result in a very high volume of debris and mud (15.000–30.000 $m^3$) mobilization due to very localized and intense rainfall. These characteristics are typical of small Mediterranean

watersheds where sudden cloudbursts are frequent in spring and autumn seasons, favoring the reactivation of alluvial fans. The flow can develop high inundation depths and transport considerable sediments, which can induce significant damage to the built environment. While physical losses to structures are often minimal due to deposition from aggradation waves that typically lack significant momentum flux, financial and functionality losses are both common and unavoidable. The most frequent damage includes breaches to doors, windows, stores, and fences, leading to flooding in ground floors, basements, gardens, and yards. Damage is predominantly limited to nonstructural elements. However, the greatest risk arises for parked vehicles and pedestrians, who could be swept away and fatally affected by the flow. Such damage can be mitigated through measures like constructing small protective walls or fences around buildings and reinforcing doors and windows.

The development of fragility curves for three nonstructural damage states represents a key contribution of this research. These curves quantify vulnerability and account for uncertainties, offering insights into damage extents specific to small Mediterranean watersheds. The analysis reveals that minor damage (DS1) is well-defined, while severe damage states (e.g., DS3) exhibit greater variability due to the complex interplay of factors driving extreme impacts. Notably, the fragility curves effectively captured the damage scenario observed during the flash flood event, making them a valuable tool for assessing flash flood impacts, physical countermeasure design, and planning resilience measures. The comparison between the proposed fragility functions and some existing vulnerability models highlights that the Southern Apennine structures are more likely to sustain damage to nonstructural elements than those reported in literature. Evidently, this study emphasizes the critical role of real-time damage and inundation depth data, obtained from post-event field surveys, in developing vulnerability curves for flash floods. The findings underscore that small catchment flash floods primarily lead to nonstructural damage, causing minimal physical losses but significant functionality disruptions in buildings, even during minor events. However, the impact of such floods is influenced by flow parameters such as velocity and peak flow rate, which cannot be directly measured but can be inferred through numerical modeling calibrated with field data such as inundation depth, debris thickness, and grain size distribution. Future research should integrate numerical and empirical analyses to include intensity measures such as momentum flux to derive flood fragility functions. A more robust vulnerability analysis is essential as losses to the built environment often surpass those at the building portfolio level. This approach can support regional flood resilience planning by incorporating vulnerability components. Being a first attempt at providing a vulnerability model tailored to this region, the derived curves serve as valuable tools for pre-flash flood planning and post-event loss assessment. Additionally, these functions can be refined and adapted for similar geological settings, aiding local stakeholders in assessing risks and formulating targeted mitigation strategies.

## CRediT authorship contribution statement

**Giovanni Forte:** Writing – review & editing, Writing – original draft, Visualization, Methodology, Investigation, Formal analysis, Data curation, Conceptualization. **Melania De Falco:** Writing – review & editing, Writing – original draft, Visualization, Software, Methodology, Investigation, Formal analysis, Data curation. **Antonio Santo:** Writing – original draft, Supervision, Investigation, Conceptualization. **Dipendra Gautam:** Writing – review & editing, Software, Methodology, Formal analysis. **Nicoletta Santangelo:** Writing – review & editing, Writing – original draft, Supervision, Resources, Project administration, Investigation, Funding acquisition, Conceptualization.

## Declaration of competing interest

The authors declare that they have no known competing financial interests or personal relationships that could have appeared to influence the work reported in this paper.

## Acknowledgments

This research was funded by FRA Project 2020 “MAFF” (Valutazione di **MA**gnitudo di eventi da **F**lash **F**lood nei Bacini torrentizi dell’Appennino meridionale) of Università degli Studi di Napoli Federico II (Principal Investigator Prof. Nicoletta Santangelo). The authors thank the regional hydrological and agrometeorological services (Centro Funzionale; Centro Agro-meteorologico, Regione Campania) for providing the rainfall data. The editor and the reviewers are gratefully acknowledged for constructive comments and discussions. Their insights have greatly improved the manuscript.

## Data availability

Data will be made available on request.

## References

Akbas, S.O., Blahut, J., Sterlacchini, S., 2009. Critical assessment of existing physical vulnerability estimation approaches for debris flows. In: Malet, J.P., Remaitre, A., Bogaard, T. (Eds.), Proceedings of Landslide Processes: From Geomorphologic Mapping to Dynamic Modelling. Strasburg, France, pp. 229–233.

Alessio, G., De Falco, M., Di Crescenzo, G., Nappi, R., Santo, A., 2013. Flood hazard of the Somma-Vesuvius region based on historical (19-20th century) and geomorphological data. Ann. Geophys. 56 (4), S0434. https://doi.org/10.4401/ag-6440.

Amato, V., Aucelli, P.P.C., Cesarano, M., Filocamo, F., Leone, N., Petrosino, P., Rosskopf, C.M., Valente, E., Casciello, E., Giralt, S., Jicha, B.R., 2018. Geomorphic response to late Quaternary tectonics in the axial portion of the Southern Apennines (Italy): a case study from the Calore River valley. Earth Surf. Process. Landf. 43 (11), 2463–2480. https://doi.org/10.1002/esp.4390.

Barredo, J.I., 2007. Major flood disasters in Europe: 1950–2005. Nat. Hazards 42, 125–148. https://doi.org/10.1007/s11069-006-9065-2.

Benito, G., Thorndycraft, V.R., 2004. Use of systematic, Palaeoflood and historical data for the improvement of flood risk Estimation: an introduction. In: Systematic, Palaeoflood and Historical Data for the Improvement of Flood Risk Estimation. Consejo Superior de Investigaciones Científicas, Madrid, Spain V.R.

Bernardini, G., Ferreira, T.M., Julia, P.B., Eudave, R.R., Quagliarini, E., 2024. Assessing the spatiotemporal impacts of users’ exposure and vulnerability to flood risk in urban built environments. Resilient Cities Soc. 100, 105043.

Borga, M., Stoffel, M., Marchi, L., Marra, F., Jakob, M., 2014. Hydrogeomorphic response to extreme rainfall in headwater systems: flash floods and debris flows. J. Hydrol. 518, 194–205.

Brenna, A., Marchi, L., Borga, L., Ghinassi, M., Zaramella, M., Surian, N., 2021. Sediment–water flows in mountain catchments: Insights into transport mechanisms as responses to high-magnitude hydrological events. J. Hydrol. 602, 126716. https://doi.org/10.1016/j.jhydrol.2021.126716.

Camarasa, A.M., Tilford, K.A., 2002. Rainfall–runoff modelling of ephemeral streams in the Valencia region (eastern Spain). Hydrol. Process. 16, 3329–3344. https://doi.org/10.1002/hyp.1103.

CARG, 2010. Note illustrative della carta geologica d’Italia alla scala 1:50000. Foglio Caserta Est 431, 140. Retrieved from. http://www.isprambiente.gov.it/Media/carg/note_illustrative/431_Caserta_est.pdf.

Chen, M., Tang, C., Zhang, X., Xiong, J., Chang, M., Shi, Q., Wang, F., Li, M., 2021. Quantitative assessment of physical fragility of buildings to the debris flow on 20 August 2019 in the Cutou gully, Wenchuan, southwestern China. Eng. Geol. 293, 106319.

Church, M., 2006. Bed material transport and the morphology of alluvial river channels. Annu. Rev. Earth Planet. Sci. 34 (1), 325–354. https://doi.org/10.1146/annurev earth.33.092203.122721.

Collier, C., 2007. Flash flood forecasting: what are the limits of predictability? Q. J. R. Meteorol. Soc. 133 (622A), 3–23.

Corniello, A., Guida, M., Stellato, L., Trifuoggi, M., Carraturo, F., Del Gaudio, E., Del Giudice, C., Forte, G., Giarra, A., Iorio, M., Marzaioli, F., Toscanesi, M., 2021. Hydrochemical, isotopic and microbiota characterization of Telese mineral waters (Southern Italy). Environ. Geochem. Health. https://doi.org/10.1007/s10653-021-00806-4.

Corominas, J., Copons, R., Moya, J., Vilaplana, J.M., Altimir, J., Amigò, J., 2005. Quantitative assessment of the residual risk in a rock fall protected area. Landslides 2, 343–357.

Corominas, J., van Westen, C., Frattini, P., Cascini, L., Malet, J.-P., Fotopoulou, S., Catani, F., Van Den Eeckhaut, M., Mavrouli, O., Agliardi, F., Pitilakis, K., Winter, M. G., 2014. Recommendations for the quantitative analysis of landslide risk. Bull. Eng. Geol. Environ. 73 (2), 209–263.

Costa, J.E., 1988. Rheologic, geomorphic and sedimentologic differentiation of water floods, hyperconcentrated flows, and debris flows. In: Baker, R.R., Kochel, R.C., Patton, C. (Eds.), Flood Geomorphology. Wiley, New York, NY, pp. 113–122.

Coussot, P., Meunier, M., 1996. - Recognition, classification and mechanical description of debris flows. Earth-Sci. Rev. 40, 209–227.

Creutin, J.D., Borga, M., 2003. Radar hydrology modifies the monitoring of flash flood hazard. Hydrol. Process. 17 (7), 1453–1456. https://doi.org/10.1002/hyp.5122.
Crow, E.L., Davis, F.A., Maxfield, M.W., 1960. Statistics Manual. Dover Publication, New York.
De Falco, M., Forte, G., Santangelo, N., Santo, A., 2016. Flash floods in torrential basins: the event of October 14th-15th 2015 in the surroundings of Benevento (Southern Italy). Rend. Online Soc. Geol. It. 41, 131–134.
De Risi, R., Jalayer, F., De Paola, F., Carozza, S., Yonas, N., Giugni, M., Gasparini, P., 2019. From flood risk mapping toward reducing vulnerability: the case of Addis Ababa. Nat. Hazards 100, 387–415.
Di Bucci, D., Massa, B., Zuppetta, A., 2006. Relay ramps in active normal fault zones: a clue to the identification of seismogenic sources (1688 Sannio earthquake, Italy). GSA Bull. 118 (3/4), 430–448. https://doi.org/10.1130/B25783.1.
Diakakis, M., Deligiannakis, G., Antoniadis, Z., Melaki, M., Katsetsiadou, N.K., Andreadakis, E., Spyrou, N.I., Gogou, M., 2020. Proposal of a flash flood impact severity scale for the classification and mapping of flash flood impacts. J. Hydrol. 590, 125452.
Dolojan, N.L.J., Moriguchi, S., Hashimoto, M., Tinh, N.X., Tanaka, H., Terada, K., 2023. Hydrologic-geotechnical modelling of shallow landslide and flood hazards caused by heavy rainfall. Eng. Geol. 323, 107184.
Eidsvig, U.M.K., Papathoma-Köhle, M., Dub, J., Glade, T., Vangelsten, B.V., 2014. Quantification of model uncertainty in debris flow vulnerability assessment. Eng. Geol. 181, 15–26.
Ferreira, T.M., Santos, P.P., 2020. An integrated approach for assessing flood risk in historic city centers. Water 12 (6), 1648.
Fuchs, S., 2008. Vulnerability to torrent processes. In: Brebbia, C., Beriatos, E. (Eds.), Risk Analysis VI. WIT Transactions on Information and Communication Technologies. WIT, Southampton.
Fuchs, S., Heiss, K., Hübl, J., 2007. Towards an empirical vulnerability function for use in debris flow risk assessment. Nat. Hazards Earth Syst. Sci. 7, 495–506.
Gaume, E., Borga, M., 2008. Post-flooded investigations in upland catchments after major flash floods: proposal of a methodology and illustrations. J. Flood Risk Manag. 1, 175–189. https://doi.org/10.1111/j.1753-318X.2008.00023.x.
Gaume, E., Bain, V., Bernardara, P., Newinger, O., Barbuc, M., Bateman, A., Viglione, A., 2009. A compilation of data on European flash floods. J. Hydrol. 367, 70–78. https://doi.org/10.1016/j.jhydrol.2008.12.028.
Gautam, D., 2018. Observational fragility functions for residential stone masonry buildings in Nepal. Bull. Earthq. Eng. 16 (10), 4661–4673.
Gautam, D., Dong, Y., 2018. Multi-hazard vulnerability of structures and lifelines due to the 2015 Gorkha earthquake and 2017 central Nepal flash flood. J. Build. Eng. 17, 196–201.
Gautam, D., Adhikari, R., Rupakhety, R., 2021. Seismic fragility of structural and Non-structural elements of Nepali RC buildings. Eng. Struct. 2321, 111879.
Gautam, D., Adhikari, R., Gautam, S., Pandey, V.P., Thapa, B.R., Lamichhane, S., et al., 2023. Unzipping flood vulnerability and functionality loss: tale of struggle for existence of riparian buildings. Nat. Hazards 119, 989–1009.
Georgakakos, K.P., 1992. Advances in forecasting flash floods. In: Proceedings of the CCNAA-AIT Joint Seminar on Prediction and Damage Mitigation of Meteorologically Induced Natural Disasters, 21–24 May 1992. National Taiwan University, Taipei, Taiwan, pp. 280–293.
Grelle, G., Rossi, A., Revellino, P., Guerriero, L., Guadagno, F.M., Sappa, G., 2019. Assessment of debris-flow erosion and deposit areas by morphometric analysis and a GIS-based simplified procedure: a case study of paupisi in the southern Apennines. Sustainability 11 (8), 2382. https://doi.org/10.3390/su11082382.
Guerriero, L., Ruzza, G., Guadagno, F.M., Revellino, P., 2020. Flood hazard mapping incorporating multiple probability models. J. Hydrol. 587, 125020. https://doi.org/10.1016/j.jhydrol.2020.125020.
Hicks, D.M., Gomez, B., 2016. Sediment transport. In: Kondolf, G.M., Piégay, H. (Eds.), Tools in Fluvial Geomorphology. John Wiley & Sons, Hoboken, NJ, pp. 324–356. https://doi.org/10.1002/9781118648551.ch15.
Hungr, O., 1997. Some methods of landslide hazard intensity mapping. In Proceedings of the Landslide Risk Workshop. Balkema, Rotterdam, The Netherlands, pp. 215–226.
Hürlimann, M., Copons, R., Altimir, J., 2006. Detailed debris flow hazard assessment in Andorra: a multidisciplinary approach. Geomorphology 78, 359–372. https://doi.org/10.1016/j.geomorph.2006.02.003.
IAHS-UNESCO-WMO (Ed.), 1974. Flash Floods: Proceedings of the Paris Symposium, September 1974, Publication, p. 112.
Kirpich, Z.P., 1940. Time of concentration of small agricultural watersheds. J. Civ. Eng. 10 (6), 362.
Lei, Y., Gu, H., Cui, P., 2022. Vulnerability assessment for buildings exposed to torrential hazards at Sichuan-Tibet transportation corridor. Eng. Geol. 308, 106803.
Lumbroso, D., Gaume, E., 2012. Reducing the uncertainty in indirect estimates of extreme flash flood discharges. J. Hydrol. 414-415, 16–30. https://doi.org/10.1016/j.jhydrol.2011.08.048.
Luo, H., Zhang, L., Wang, H., He, J., 2020. Multi-hazard vulnerability of buildings to debris flows. Eng. Geol. 279, 105859.
Magliulo, P., Cusano, A., 2016. Geomorphology of the lower Calore River alluvial plain (Southern Italy). J. Maps 12 (5), 1119–1127. https://doi.org/10.1080/17445647.2015.1132277.
Mavrouli, O., Corominas, J., 2010. Vulnerability of simple reinforced concrete buildings to damage by rockfalls. Landslides 7 (2), 169–180.
Mavrouli, O., Fotopoulou, S., Pitilakis, K., Zuccaro, G., Corominas, J., Santo, A., Cacace, F., De Gregorio, D., Di Crescenzo, G., Foerster, E., Ulrich, T., 2014. Vulnerability assessment for reinforced concrete buildings exposed to landslides. Bull. Eng. Geol. Environ. 73 (2), 265–289.
Miano, A., Jalayer, F., Forte, G., Santo, A., 2020. Empirical fragility assessment using conditional GMPE-based ground shaking fields: application to damage data for 2016 Amatrice Earthquake. Bull. Earthq. Eng. 18 (15), 6629–6659. https://doi.org/10.1007/s10518-020-00945-6.
Miranda, F.N., Ferreira, T.M., 2019. A simplified approach for flood vulnerability assessment of historic sites. Nat. Hazards 96, 713–730.
National Research Council, 1996. Alluvial Fan Flooding. National Academy Press, Washington, DC, pp. 1–131.
Palumbo, M., Ascione, A., Santo, A., Santangelo, N., 2024. Evaluation of sediment budgets in catchments prone to flash flood-related debris flows: a case study from the southern Apennines (Italy). Geomorphology 454, 109174. https://doi.org/10.1016/j.geomorph.2024.109174.
Papathoma-Köhle, M., Keiler, M., Totschnig, R., Glade, T., 2012. Improvement of vulnerability curves using data from extreme events: debris flow event in South Tyrol. Nat. Hazards 64, 2083–2105. https://doi.org/10.1007/s11069-012-0105-9.
Papathoma-Köhle, M., Schlögl, M., Dosser, L., Roesch, F., Borga, M., Erlicher, M., Keiler, M., Fuchs, S., 2022. Physical vulnerability to dynamic flooding: vulnerability curves and vulnerability indices. J. Hydrol. 607, 127501. https://doi.org/10.1016/j.jhydrol.2022.127501.
Parisi, F., Sabella, G., 2017. Flow-type landslide fragility of reinforced concrete framed buildings. Eng. Struct. 131, 28–43. https://doi.org/10.1016/j.engstruct.2016.10.013.
Patacca, E., Scandone, P., 2007. Geology of the southern Apennines. Boll. Soc. Geol. Ital. 7, 75–119.
Petrone, C., Rossetto, T., Goda, K., 2017. Fragility assessment of a RC structure under tsunami actions via nonlinear static and dynamic analyses. Eng. Struct. 136, 36–53.
Pierson, T.C., 2005. Distinguishing between debris flows and floods from field evidence in small watersheds: USGS Fact Sheet 2004-3142, p. 4. Retrieved from. http://pubs.usgs.gov/fs/2004/3142/.
Pierson, T.C., Costa, J.E., 1987. A rheologic classification of subaerial sediment-water flows. Geol. Soc. Am. Rev. Eng. Geol. 7, 1–12.
Quan Luna, B., Blahut, J., Van Westen, C.J., Sterlacchini, S., Van Asch, T.W.J., Akbas, S. O., 2011. The application of numerical debris flow modelling for the generation of physical vulnerability curves. Nat. Hazards Earth Syst. Sci. 11, 2047–2060.
Ruiz-Villanueva, V., Bodoque, J.M., Díez-Herrero, A., Eguibar, M.A., Pardo-Igúzquiza, E., 2013. Reconstruction of a flash flood with large wood transport and its influence on hazard patterns in an ungauged mountain basin. Hydrol. Process. 27, 3424–3437. https://doi.org/10.1002/hyp.9433.
Santangelo, N., Daunis-i-Estadella, J., Di Crescenzo, G., Di Donato, V., Faillace, P., Martin-Fernandez, J.A., Scorpio, V., 2012. Topographic predictors of susceptibility to alluvial fan flooding, southern Apennines. Earth Surf. Process. Landf. 37, 803–817. https://doi.org/10.1002/esp.3197.
Santangelo, N., Forte, G., De Falco, M., Chirico, G.B., Santo, A., 2021. New insights on rainfall triggering flow-like landslides and flash floods in Campania (Southern Italy). Landslides 18 (8), 2923–2933.
Santo, A., Ascione, A., Del Prete, S., Di Crescenzo, G., Santangelo, N., 2011. Collapse sinkholes distribution in the carbonate massifs of central and southern Apennines. Acta Carsol. 40 (1), 95–112. https://doi.org/10.3986/ac.v40i1.31.
Santo, A., Santangelo, N., Di Crescenzo, G., Scorpio, V., De Falco, M., Chirico, G.B., 2015. Flash flood occurrence and magnitude assessment in an alluvial fan context: the October 2011 event in the Southern Apennines. Nat. Hazards. https://doi.org/10.1007/s11069-015-1728-4.
Santo, A., Santangelo, N., Forte, G., De Falco, M., 2016. Post flash flood survey: the 14th and 15th October 2015 event in the Paupisi-Solopaca area (Southern Italy). J. Maps 13 (2), 19–25.
Santo, A., Santangelo, N., Balassone, G., Strauss, H., 2019. Deep seated fault-related volcanogenic H 2 S as the key agent of high sinkhole concentration areas. Earth Surf. Process. Landf. 44 (3), 713–735. https://doi.org/10.1002/esp.4526.
Sun, X., Zeng, P., Li, T., Jimenez, R., Xu, Q., Zhang, L., 2023. Probabilistic framework to evaluate scenario-based building vulnerability under landslide run-out impacts. Eng. Geol. 325, 107274.
Thapa, S., Shrestha, A., Lamichhane, S., Adhikari, R., Gautam, D., 2020. Catchment-scale flood hazard mapping and flood vulnerability analysis of residential buildings: the case of Khando River in eastern Nepal. J. Hydrol. Reg. Stud. 30, 100704. https://doi.org/10.1016/j.ejrh.2020.100704.
Totschnig, R., Sedlacek, W., Fuchs, S., 2011. A quantitative vulnerability function for fluvial sediment transport. Nat. Hazards 58, 681–703.
Uzielli, M., Nadim, F., Lacasse, S., Kaynnia, A., 2008. A conceptual framework for quantitative estimation of physical vulnerability to landslides. Eng. Geol. 102 (3–4), 251–256.
Van Dine, D.F., 1985. Debris flows and debris torrents in the southern Canadian Cordillera. Can. Geotech. J. 22 (1), 44–68. https://doi.org/10.1139/t85-006.
Vennari, C., Parise, M., Santangelo, N., Santo, A., 2016. A database on flash flood events in Campania, southern Italy, with an evaluation of their spatial and temporal distribution. Nat. Hazards Earth Syst. Sci. 16 (12), 2485–2500.
Wilford, D.J., Sakals, M.E., Innes, J.L., Sidle, R.C., Bergerud, W.A., 2004. Recognition of debris flow, debris flood and flood hazard through watershed morphometrics. Landslides 1, 61–66. https://doi.org/10.1007/s10346-003-0002-0.
Yan, S., He, S., Deng, Y., Liu, W., Wang, D., Shen, F., 2020. A reliability-based approach for the impact vulnerability assessment of bridge piers subjected to debris flows. Eng. Geol. 269, 105567.
Zhang, S., Zhang, L., Lib, X., Xuc, Q., 2018. Physical vulnerability models for assessing building damage by debris flows. Eng. Geol. 247, 145–158.